T. Luo, M. Xu, C. Colombo
Heliotropic Frozen Orbits Design for High Area-To-mass Ratio Spacecraft
Journal of Astronomical Telescopes, Instruments, and Systems, Vol. 5, N. 3, 2019, 036003 (12 pages)
doi:10.1117/1.JATIS.5.3.036003

Heliotropic Frozen Orbits Design for High Area-to-Mass Ratio Spacecraft

Tong Luo[1], Ming Xu[2], Camilla Colombo[3]

[1, 2] School of Astronautics, Beihang University, Beijing 100191, China.

[3] Department of Aerospace Science and Technology, Politecnico di Milano, Milano 20156, Italy

Abstract

Heliotropic orbits and frozen orbits both possess unique advantages in Earth observation missions and communication service. However, few scholars have found an orbit which possesses heliotropic and frozen characteristics at the same time. This paper obtains novel heliotropic frozen orbits through a proposed control strategy, which is accomplished by adjusting the area-to-mass ratio and the attitude angles. First, we construct the dynamical model of high area-to-mass ratio spacecraft under the effect of J_2 perturbation and solar radiation pressure. Then, nominal heliotropic frozen orbits are solved by assuming that the obliquity angle of the ecliptic with respect to the equator is zero. Finally, a control strategy is proposed to maintain heliotropic frozen orbits when the obliquity angle of the ecliptic with respect to the equator is considered. In addition, practical examples are provided to verify the heliotropic and frozen characteristics and the robustness of the controlled orbits. Orbit design for Earth observation and communication service is also studied.

Key Words: Heliotropic frozen orbits; High area-to-mass ratio spacecraft; J_2 perturbation; Solar

---

[1] PhD candidate, School of Astronautics, Beihang University, luotong@buaa.edu.cn.

[2] Associate professor, School of Astronautics, Beihang University, xuming@buaa.edu.cn (Corresponding Author).

[3] Associate professor, Department of Aerospace Science and Technology, Politecnico di Milano, camilla.colombo@polimi.it.

radiation pressure

1. Introduction

Benefiting from the developments in microelectromechanical systems, an innovative spacecraft concept “smart dust” is proposed. The microchips in smart dust can offer the capabilities of sensing, computing, and communication, and the small size of smart dust can reduce production costs, favours standardization, and overcomes the limitations imposed by launch and deployment costs. Thus, smart dust has many potential applications, including global sensing networks for Earth observation [1], Earth climate engineering [2], geomagnetic exploration [3], and communication systems for conventional spacecraft operating in the interplanetary space [4]. In addition, solar sailing technology can propel a spacecraft to high speed via solar radiation pressure (SRP) [5]. The advantage that solar sail can provide a continuous acceleration limited only by the lifetime of the sail materials in the space environment makes it a perfect option for deep space exploration. Since 2010, several solar sail spacecraft missions have been completed, such as NanoSail-D2 [6], the Interplanetary Kite-Craft Accelerated by Radiation of the Sun (IKAROS) [7], and LightSail1 [8].

Smart dust has a characteristic side length of some centimeters or ever some millimeters, while solar sail has a very large area. As a result, they both possess high area-to-mass ratio property and will motion on a non-Keplerian orbit under the effect of perturbations, such as SRP [9], atmospheric drag [10], and electrostatic forces [11]. Colombo and McInnes [12] obtained long-term equilibrium orbits for a space-chip device by balancing the perturbations due to solar radiation and atmospheric drag. Früh and Jah [13] proposed a semi-coupled approach for propagating the attitude and orbital dynamics of objects near the geostationary ring. Zhao et al. [14] investigated the long-term evolution of the smart

dust's orbit with the consideration of the gravitational potential. Mengali et al. [15] [16] studied the heliocentric dynamics of sun-pointing smart dust which can provide an outward propulsive acceleration directed along the sun-smart dust line.

Because the apogee of a heliotropic orbit always points in the direction of the Sun, spacecraft motioning on this orbit will spend the largest portion of time on the Sun facing side of the orbit. Colombo and McInnes [17] constructed constellations of heliotropic orbits for enhanced earth coverage. Lantukh et al. [18] proposed a constrained double averaging method to solve the semi-analytical solutions of inclined heliotropic orbits at oblate asteroids. Later, Russell et al. [19] also adopted the constrained double averaging method and obtained more precise solutions of heliotropic orbits by considering zonal harmonics and simple shadowing. However, the above heliotropic orbits are all obtained by assuming that the obliquity angle of the "ecliptic" with respect to the "equator" is zero. As for frozen orbits, their greatest advantages are that the variations of orbital elements are theoretically zero and the effort for orbit maintenance can be reduced [20]. Thus, many Earth observation missions, such as SEASATA, LANDSAT, GEOSAT, SPOT, ERS, and Topex/Poseidon, were all placed into a frozen orbit [21] [22]. In addition, the frozen orbit can also be applied to a lunar mapping mission [23] and swarm mission [24].

Heliotropic orbit and frozen orbit have been widely studied because of their advantages and potential applications. However, few scholars have found an orbit which possesses heliotropic and frozen characteristic at the same time. This paper focuses on the motion of high area-to-mass ratio spacecraft on medium earth orbit where it is mainly perturbed by J_2 and SRP. Considering the obliquity angle of the ecliptic with respect to the equator, no natural heliotropic frozen orbit can be theoretically solved from the dynamical equations. Then, we obtain novel heliotropic frozen orbits through a

proposed control strategy which is accomplished by adjusting the area-to-mass ratio and the attitude angles. This paper is organized as follows. Section 2 constructs the dynamical model of high area-to-mass ratio spacecraft under the effect of J_2 and SRP. Section 3 gives solutions of nominal heliotropic frozen orbits by ignoring the obliquity angle of the ecliptic with respect to the equator. Section 4 proposes a control strategy to maintain the nominal heliotropic frozen orbits, verifies the control strategy through practical examples, and studies the robustness, applications of the controlled heliotropic frozen orbits.

2. Dynamical model

2.1. Disturbing potential functions

The motion of high area-to-mass ratio spacecraft orbiting the Earth is markedly perturbed by the oblateness of Earth and SRP. According to ref [25], the orbit-average disturbing function associated with Earth's oblateness J_2 is

$$\begin{aligned} \left\langle R_{obl} \right\rangle &= W n_{sun} \frac{n a^2}{6} \frac{3\cos^2 i - 1}{(1-e^2)^{3/2}}, \\ W &= \frac{3}{2} J_2 \frac{R^2}{a^2} \frac{n}{n_{sun}}, \end{aligned} \tag{1}$$

where W is oblateness parameter, n is the mean motion velocity of the spacecraft, J_2 is the second zonal coefficient, R is the equatorial radius of the Earth, and n_{sun} is the orbital angular velocity of the Earth around the Sun (circular Earth orbit is adopted).

The disturbing potential function associated with SRP is closely related to the normal vector of the spacecraft's sail. To determine the orientation of the normal vector, we can define two coordinate systems, namely the inertial coordinate system S_g and body coordinate system S_b. As shown in Fig. 1, the origin of S_g is located at the center of the Earth, the x-axis of S_g points to the vernal equinox, the z-

axis of S_g points to the North Pole, and the y-axis of S_g is determined by the right-hand rule. The origin of S_b is located at the center of the Earth, and the x-axis of S_b is along the normal vector of the spacecraft's sail. S_b can be obtained through two basic coordinate rotations from S_g, namely $S_g \xrightarrow{\mathbf{L}_x(\varepsilon)} \circ \xrightarrow{\mathbf{L}_z(\lambda)} S_b$, where two rotation angles ε and λ are shown in the spherical triangle of Fig. 1. Thus, the coordinate transformation matrix from S_b to S_g is obtained as

$$\mathbf{L}_{gb} = \mathbf{L}_x(-\varepsilon)\mathbf{L}_z(-\lambda) = \begin{bmatrix} 1 & 0 & 0 \\ 0 & \cos\varepsilon & -\sin\varepsilon \\ 0 & \sin\varepsilon & \cos\varepsilon \end{bmatrix} \begin{bmatrix} \cos\lambda & -\sin\lambda & 0 \\ \sin\lambda & \cos\lambda & 0 \\ 0 & 0 & 1 \end{bmatrix} = \begin{bmatrix} \cos\lambda & \cdots & \cdots \\ \cos\varepsilon\sin\lambda & \cdots & \cdots \\ \sin\varepsilon\sin\lambda & \cdots & \cdots \end{bmatrix}. \tag{2}$$

According to Ref [5], the SRP acceleration can be expressed as

$$\begin{aligned} \mathbf{a}_{srp} &= p_{srp}\eta\cos^2\alpha\cdot\mathbf{n}, \\ \eta &= c_r\frac{A_{sun}}{m}, \end{aligned} \tag{3}$$

where p_{srp} denotes the SRP on unit area's sail, c_r denotes the sail's reflectivity coefficient dependent on sail's material, A_{sun} denotes the sail's area exposed to the Sun, m denotes the mass of the spacecraft, η denotes the spacecraft's effective area-to-mass ratio, $\mathbf{n}$ denotes the unit normal vector of sail surface in S_b, and α denotes the angle between the Earth-Sun line and the sail's normal vector (the vector directed from the Sun to the spacecraft's center is assumed the same with the Sun-Earth line direction because the distance between the spacecraft and Earth can be ignored compared to the distance between Sun and Earth). Based on the definition of S_b, $\mathbf{n}$ is exactly the opposite direction of the x-axis of S_b and can be expressed as

$$\{\mathbf{n}\}_b = \begin{bmatrix} -1 & 0 & 0 \end{bmatrix}^T. \tag{4}$$

Then, the expression of $\mathbf{n}$ in S_g can be obtained as

$$\{\mathbf{n}\}_g = \mathbf{L}_{gb}\{\mathbf{n}\}_b = \begin{bmatrix} \cos\lambda & \cdots & \cdots \\ \cos\varepsilon\sin\lambda & \cdots & \cdots \\ \sin\varepsilon\sin\lambda & \cdots & \cdots \end{bmatrix} \begin{bmatrix} -1 \\ 0 \\ 0 \end{bmatrix} = -\begin{bmatrix} \cos\lambda \\ \cos\varepsilon\sin\lambda \\ \sin\varepsilon\sin\lambda \end{bmatrix}. \tag{5}$$

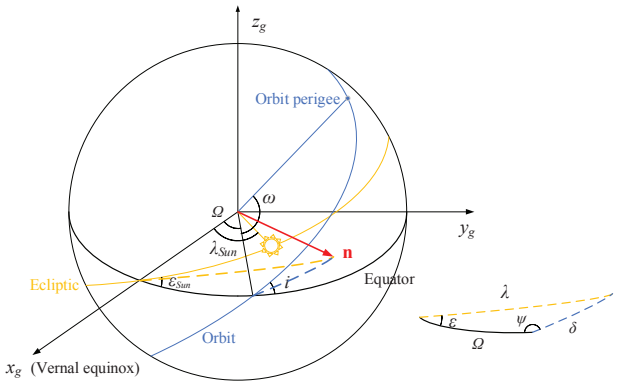

Fig. 1. The three-dimensional geometric diagram for a high area-to-mass ratio spacecraft's orbit.

Because the SRP acceleration is the gradient of disturbing potential function, the corresponding function can be derived as

$$R_{srp} = -p_{srp}\eta\cos^2\alpha\left(x\cos\lambda + y\cos\varepsilon\sin\lambda + z\sin\varepsilon\sin\lambda\right), \tag{6}$$

where (x, y, z) is the coordinate position of the spacecraft in S_g. The values of x, y, and z are related to orbital elements by following equations

$$\begin{aligned} x &= r\left(\cos(\omega+f)\cos\Omega - \sin(\omega+f)\sin\Omega\cos i\right), \\ y &= r\left(\cos(\omega+f)\sin\Omega + \sin(\omega+f)\sin\Omega\cos i\right), \\ z &= r\sin(\omega+f)\sin i, \end{aligned} \tag{7}$$

where r is the real-time distance between the spacecraft and Earth, ω is the argument of pericenter, f is the true anomaly, Ω is longitude of the node, and i is orbital inclination with respect to the equatorial plane. Substituting Eqs. (7) into Eq. (6) and performing the average method in orbit, we can obtain orbit-average disturbing function with SRP as

$$\begin{aligned} \left\langle R_{srp}\right\rangle &= C_{srp}n_{sun}na^2e\cos^2\alpha\left(\begin{array}{l}\cos\omega\left(\cos\Omega\cos\lambda+\sin\Omega\cos\varepsilon\sin\lambda\right)+\\ \sin\omega\left(-\sin\Omega\cos i\cos\lambda+\cos\Omega\cos i\sin\lambda\cos\varepsilon+\sin i\sin\varepsilon\sin\lambda\right)\end{array}\right), \\ C_{srp} &= \frac{3}{2}p_{srp}\eta\frac{a^2}{\mu_{Earth}}\frac{n}{n_{sun}}, \end{aligned} \tag{8}$$

where C_{srp} is a radiative parameter. With the application of spherical trigonometry to the spherical triangle in Fig. 1, Eq. (8) can be simplified into

$$\left\langle R_{srp} \right\rangle = C_{srp} n_{sun} n a^2 e \cos^2 \alpha \left(\cos\omega \cos\delta - \sin\omega \sin\delta \cos\left(i+\psi\right) \right), \tag{9}$$

2.2. Lagrange planetary equations

The change rates of orbital elements can be expressed by Lagrange planetary equations [26], which are given by

$$\begin{aligned}
\dot{a} &= \frac{2}{na}\frac{\partial R}{\partial M}, \\
\dot{e} &= -\frac{\sqrt{1-e^2}}{ena^2}\frac{\partial R}{\partial \omega}, \\
\dot{i} &= \frac{\cot i}{na^2\sqrt{1-e^2}}\frac{\partial R}{\partial \omega} - \frac{\csc i}{na^2\sqrt{1-e^2}}\frac{\partial R}{\partial \Omega}, \\
\dot{\Omega} &= \frac{\csc i}{na^2\sqrt{1-e^2}}\frac{\partial R}{\partial i}, \\
\dot{\omega} &= \frac{\sqrt{1-e^2}}{ena^2}\frac{\partial R}{\partial e} - \frac{\cot i}{na^2\sqrt{1-e^2}}\frac{\partial R}{\partial i}, \\
\dot{M} &= n - \frac{2}{na}\frac{\partial R}{\partial a} - \frac{1-e^2}{ena^2}\frac{\partial R}{\partial e},
\end{aligned} \tag{10}$$

where R is the disturbing function. Inserting Eqs. (1) and (9) into Eqs. (10), we can derive the change rates of orbital elements as

$$\begin{aligned}
\dot{a} &= 0, \\
\dot{e} &= \sqrt{1-e^2} C_{srp} n_{sun} \cos^2\alpha \left(\sin\omega\cos\delta + \cos\omega\sin\delta\cos\left(i+\psi\right) \right), \\
\dot{i} &= \frac{e}{\sqrt{1-e^2}} C_{srp} n_{sun} \cos^2\alpha \cos\omega \sin\delta \frac{\cos\psi - \cos i \cos\left(i+\psi\right)}{\sin i}, \\
\dot{\Omega} &= -\frac{W n_{sun}}{\left(1-e^2\right)^2}\cos i + \frac{e}{\sqrt{1-e^2}} C_{srp} n_{sun} \cos^2\alpha \sin\omega \sin\delta \frac{\sin\left(i+\psi\right)}{\sin i}, \\
\dot{\omega} &= \frac{W n_{sun}}{\left(1-e^2\right)^2}\frac{5\cos^2 i - 1}{2} + C_{srp} n_{sun} \cos^2\alpha \begin{pmatrix} \frac{\sqrt{1-e^2}}{e}\left(\cos\omega\cos\delta - \sin\omega\sin\delta\cos\left(i+\psi\right)\right) \\ -\frac{e}{\sqrt{1-e^2}}\sin\omega\sin\delta\frac{\cos i \sin\left(i+\psi\right)}{\sin i} \end{pmatrix}, \\
\dot{M} &= n - \frac{5}{3}\frac{W n_{sun}}{\left(1-e^2\right)^{3/2}}\left(3\cos^2 i - 1\right) - \left(4e + \frac{1-e^2}{e}\right) C_{srp} n_{sun} \cos^2\alpha \left(\cos\omega\cos\delta - \sin\omega\sin\delta\cos\left(i+\psi\right) \right).
\end{aligned} \tag{11}$$

We define a characteristic angle $\Pi = \omega + \kappa_{dir}(\Omega - \lambda_{sun})$ to describe the orientation of the spacecraft respect to the Sun. The retrograde factor κ_{dir} is determined as $\kappa_{dir}=1$ for prograde orbits and $\kappa_{dir}=-1$ for

retrograde orbits. Then an orbit is heliotropic when $\Pi = \pm\pi$, while anti-heliotropic when $\Pi = 0$. Thus, heliotropic frozen orbits require the orbital elements to satisfy

$$\begin{aligned} &\dot{e} = 0, \quad \dot{i} = 0, \quad \dot{\omega} = 0, \\ &\dot{\Omega} - n_{sun} = 0, \quad \Pi = \pm\pi, \end{aligned} \tag{12}$$

where the first three equations are the conditions for frozen characteristic, and the last two are the conditions for heliotropic characteristic.

3. Nominal heliotropic frozen orbits

Because variables Ω, δ, and ψ will change irregularly in general cases, no analytical solutions exist for Eqs. (12). To obtain possible solutions of heliotropic frozen orbits, we will simplify the problem through following assumptions. Suppose that the normal vector of the spacecraft's sail is always along the Earth-Sun line, and the obliquity angle of the ecliptic with respect to the equator is zero, we will obtain α=0, ε=0, λ=λ_{sun}, ε_{sun}=0, ψ=π, and δ=λ_{sun}-Ω. Then the change rates of e, i, ω, and Ω are simplified into

$$\begin{aligned} \dot{e} &= \sqrt{1-e^2}\, C_{srp} n_{sun} \left(\sin\omega\cos\delta - \cos\omega\sin\delta\cos i\right), \\ \dot{i} &= -\frac{e}{\sqrt{1-e^2}} C_{srp} n_{sun} \cos\omega\sin\delta\sin i, \\ \dot{\Omega} &= -\frac{W n_{sun}}{\left(1-e^2\right)^2}\cos i - \frac{e}{\sqrt{1-e^2}} C_{srp} n_{sun} \sin\omega\sin\delta, \\ \dot{\omega} &= \frac{W n_{sun}}{\left(1-e^2\right)^2}\frac{5\cos^2 i - 1}{2} + C_{srp} n_{sun} \left(\begin{array}{l} \dfrac{\sqrt{1-e^2}}{e}\left(\cos\omega\cos\delta + \sin\omega\sin\delta\cos i\right) \\ + \dfrac{e}{\sqrt{1-e^2}}\sin\omega\sin\delta\cos i \end{array} \right). \end{aligned} \tag{13}$$

Based on the conditions $\dot{e} = 0$ and $\dot{i} = 0$ in Eqs. (12), we derive the following constraints for variables ω and δ:

$$\sin\omega\cos\delta = 0, \quad \cos\omega\sin\delta = 0. \tag{14}$$

Eight groups feasible values of ω and δ can be solved from Eqs. (14), and we summary them in the

following table.

Table 1. Eight groups feasible values of ω and δ

(ω, δ)	$\cos\omega\cos\delta$	$\sin\omega\sin\delta$	heliotropic orbits	anti-heliotropic orbits
$(0, 0)$ or (π, π)	1	0	none	all
$(0, \pi)$ or $(\pi, 0)$	-1	0	all	none
$(\frac{\pi}{2}, \frac{\pi}{2})$ or $(-\frac{\pi}{2}, -\frac{\pi}{2})$	0	1	$i>\frac{\pi}{2}$	$i<\frac{\pi}{2}$
$(\frac{\pi}{2}, -\frac{\pi}{2})$ or $(-\frac{\pi}{2}, \frac{\pi}{2})$	0	-1	$i<\frac{\pi}{2}$	$i>\frac{\pi}{2}$

As shown in Table 1, eight groups of feasible values are divided into four different cases according to the values of $\cos\omega\cos\delta$ and $\sin\omega\sin\delta$. When $\cos\omega\cos\delta=1$ and $\sin\omega\sin\delta=0$, all solutions are anti-heliotropic orbits. Thus we do not study this case in the following part. When $\cos\omega\cos\delta=-1$ and $\sin\omega\sin\delta=0$, all solutions are heliotropic orbits. When $\cos\omega\cos\delta=0$ and $\sin\omega\sin\delta=1$, retrograde orbits are heliotropic orbit. When $\cos\omega\cos\delta=0$ and $\sin\omega\sin\delta=-1$, prograde orbits are heliotropic orbits. Because of $\delta=\lambda_{sun}-\Omega$, conditions $\dot{\Omega}-n_{sun}=0$ and $\dot{\omega}=0$ can guarantee that the values of δ and ω are both constant. Thus, we can obtain possible solutions of heliotropic frozen orbits by solving $\dot{\Omega}-n_{sun}=0$ and $\dot{\omega}=0$ for different cases.

Case 1: $\cos\omega\cos\delta=-1$ and $\sin\omega\sin\delta=0$

In this case, constraints $\dot{\Omega}-n_{sun}=0$ and $\dot{\omega}=0$ are expressed as

$$\begin{aligned} &-\frac{Wn_{sun}}{\left(1-e^2\right)^2}\cos i-n_{sun}=0, \\ &\frac{Wn_{sun}}{\left(1-e^2\right)^2}\frac{5\cos^2 i-1}{2}-\frac{\sqrt{1-e^2}}{e}C_{srp}n_{sun}=0. \end{aligned} \tag{15}$$

When semi-major axis a and the spacecraft's area-to-mass ratio η are given, we can obtain the values

of e and i for a heliotropic frozen orbit by solving Eqs. (15). Fig. 2a demonstrates the relationship between e and a for different area-to-mass ratios, and Fig. 2b demonstrates the relationship between i and a for different area-to-mass ratios. Notice that the shadow area in Fig. 2a denotes the orbits which may be effected by the atmosphere or collide with the Earth because their perigees are too close to the Earth or below the surface of the Earth. According to the results, we can divide the values of a into three segments, namly $a<a_1$, $a_1\leq a\leq a_2$, and $a>a_2$. When $a<a_1$, no heliotropic frozen orbit exists. When $a_1\leq a\leq a_2$, the heliotropic frozen orbits have two branches A and B. These two branches share the same heliotropic frozen orbit at the boundary value a_1. For branch A, e increases and i slowly decreases with the increasing a. For branch B, e decreases and i rapidly increases with the increasing a. When $a>a_2$, branch B vanishes because the inclination cannot exceed 180 degrees, while branch A still exists. In addition, the boundary value a_1 remarkably increases with the increasing area-to-mass ratio, while the boundary value a_2 slowly increases with the increasing area-to-mass ratio. Thus, the second segment $a_1<a<a_2$ where two heliotropic frozen orbits exist become shorter with the increasing area-to-mass ratio.

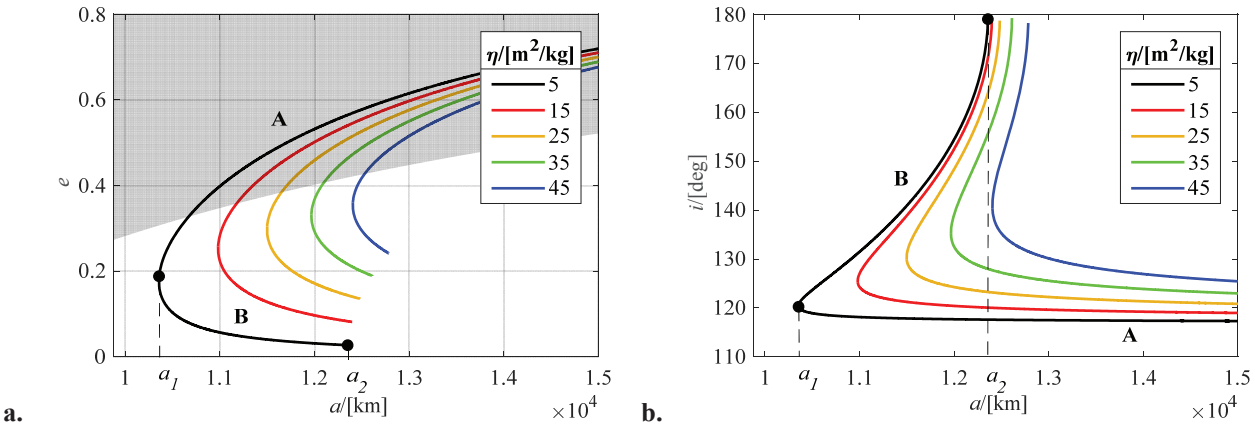

Fig. 2. a. the relationship between e and a in Case 1; b. the relationship between i and a in Case 1.

Case 2: cosωcosδ=0 and sinωsinδ=1

In this case, constraints $\dot{\Omega} - n_{sun} = 0$ and $\dot{\omega} = 0$ are expressed as

$$\begin{aligned} &-\frac{Wn_{sun}}{\left(1-e^2\right)^2}\cos i - \frac{e}{\sqrt{1-e^2}}C_{srp}n_{sun} - n_{sun} = 0, \\ &\frac{Wn_{sun}}{\left(1-e^2\right)^2}\frac{5\cos^2 i - 1}{2} + \frac{1}{e\sqrt{1-e^2}}C_{srp}n_{sun}\cos i = 0. \end{aligned} \tag{16}$$

Similar to Case 1, we obtain heliotropic frozen orbits by solving Eqs. (16). Fig. 3a and b describe the same relationships as Fig. 2a and b, respectively. According to the results, we can also divide the values of a into three segments, namly $a<a_1$, $a_1 \le a \le a_2$, and $a>a_2$. When $a<a_1$, no heliotropic frozen orbit exists. When $a_1 \le a \le a_2$, the heliotropic frozen orbits also have two branches A and B, and the trends of two branches are the same with those in Fig. 2. When $a>a_2$, branch B also vanishes, but branch A still exists. In this case, although the boundary value a_1 remarkably increases with the increasing area-to-mass ratio, the boundary value a_2 is almost invariable with the increasing area-to-mass ratio.

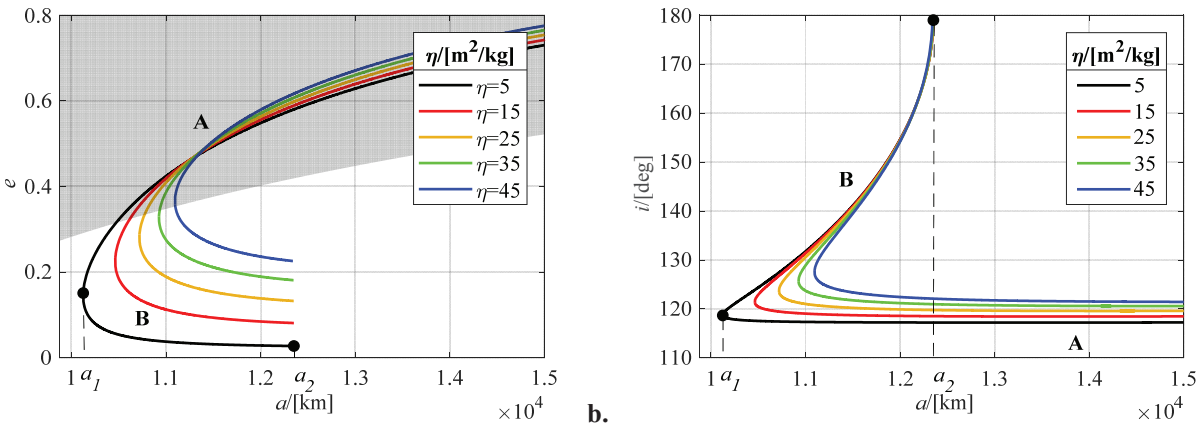

Fig. 3. a. the relationship between e and a in Case 2; b. the relationship between i and a in Case 2.

Case 3: cosωcosδ=0 and sinωsinδ=-1

In this case, constraints $\dot{\Omega} - n_{sun} = 0$ and $\dot{\omega} = 0$ are expressed as

$$
\begin{aligned}
&-\frac{Wn_{sun}}{\left(1-e^2\right)^2}\cos i+\frac{e}{\sqrt{1-e^2}}C_{srp}n_{sun}-n_{sun}=0,\\
&\frac{Wn_{sun}}{\left(1-e^2\right)^2}\frac{5\cos^2 i-1}{2}-\frac{1}{e\sqrt{1-e^2}}C_{srp}n_{sun}\cos i=0.
\end{aligned}
\tag{17}
$$

Similar to Case 1 and Case 2, we obtain heliotropic frozen orbits by solving Eqs. (17). Fig. 4a and b describe the same relationships as Fig. 2a and b, respectively. Different from the above two cases, the heliotropic frozen orbits never have two branches with the increasing semi-major axis. Fig. 4b demonstrates that the inclinations are all larger than 90 degrees. However, retrograde orbits are anti-heliotropic orbits in this case. Thus, no heliotropic orbit exists in this case.

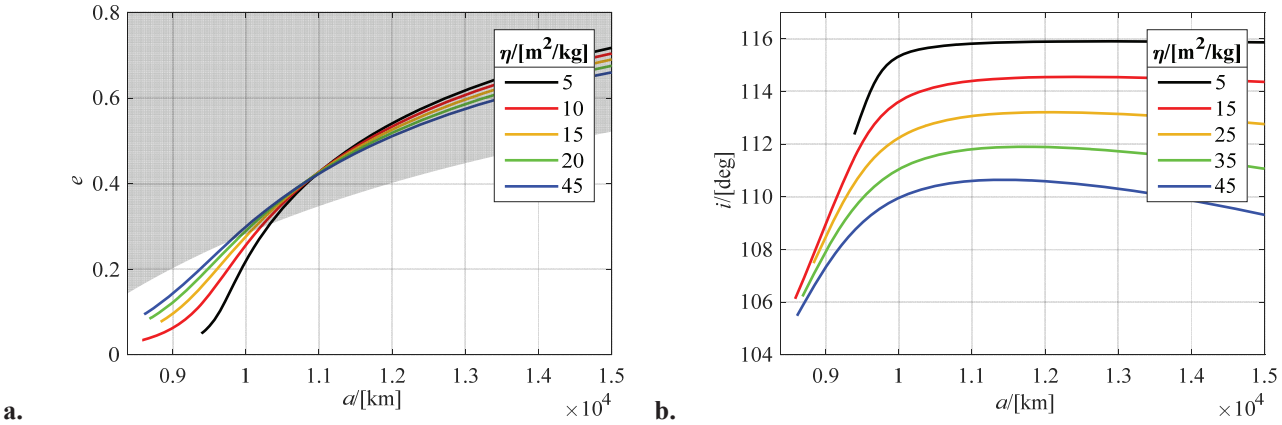

Fig. 4. a. the relationship between e and a in Case 3; b. the relationship between i and a in Case 3.

In summary, we can obtain heliotropic frozen orbits in **Case 1** and **Case 2**, but only anti-heliotropic frozen orbits in **Case 3**. In addition, all those frozen orbits are retrograde orbits. Because the heliotropic frozen orbits are solved by ignoring the obliquity angle of the ecliptic with respect to the equator, we call them nominal heliotropic frozen orbits.

4. Controlled heliotropic frozen orbits

4.1. Control strategy

The nominal heliotropic frozen orbits cannot be naturally maintained when the obliquity angle of

the ecliptic with respect to the equator is considered. However, we discover that if the normal vector of the spacecraft's sail is controlled in the equator plane, the spherical triangle in Fig. 1 will also degenerate into an arc on the equator. Then we can obtain ε=0 and ψ=π, and the change rates of e, i, ω, and Ω are simplified into

$$\begin{aligned}
\dot{e} &= \sqrt{1-e^2}\,C_{srp}n_{sun}\cos^2\alpha\left(\sin\omega\cos\delta-\cos\omega\sin\delta\cos i\right),\\
\dot{i} &= -\frac{e}{\sqrt{1-e^2}}C_{srp}n_{sun}\cos^2\alpha\cos\omega\sin\delta\sin i,\\
\dot{\Omega} &= -\frac{Wn_{sun}}{\left(1-e^2\right)^2}\cos i-\frac{e}{\sqrt{1-e^2}}C_{srp}n_{sun}\cos^2\alpha\sin\omega\sin\delta,\\
\dot{\omega} &= \frac{Wn_{sun}}{\left(1-e^2\right)^2}\frac{5\cos^2 i-1}{2}+C_{srp}n_{sun}\cos^2\alpha\left(\begin{array}{l}\dfrac{\sqrt{1-e^2}}{e}\left(\cos\omega\cos\delta+\sin\omega\sin\delta\cos i\right)\\ +\dfrac{e}{\sqrt{1-e^2}}\sin\omega\sin\delta\cos i\end{array}\right).
\end{aligned} \tag{18}$$

Here the normal vector of the spacecraft's sail is no longer along the Earth-Sun line. Compared to Eqs. (13), Eqs. (18) include the effect of angle α on the orbital elements. To quantitatively describe the angle α, we define two attitude angles β and γ. As shown in Fig. 5, β denotes the angle between the Earth-Sun line and its projection on the equator, and γ denotes the angle between the projection of the Earth-Sun line on the equator and the normal vector of the spacecraft's sail. Thus, the angles α, β, and γ have the following relationship:

$$\cos\alpha=\cos\beta\cos\gamma. \tag{19}$$

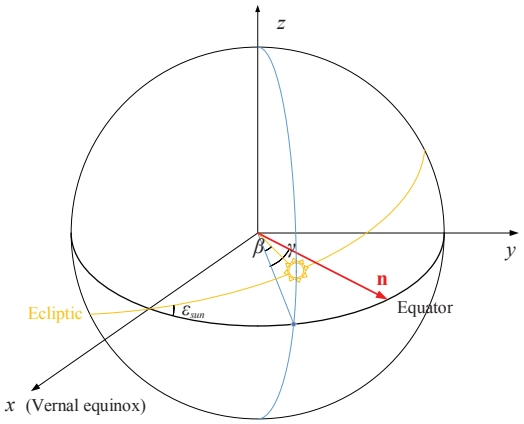

Fig. 5. Diagram of two attitude angles β and γ.

Based on the conditions $\dot{e}=0$ and $\dot{i}=0$, we derive the same constraints as Eqs. (14) for variables ω and δ. Thus, the eight groups feasible values of ω and δ in Table 1 can be also obtained. Because the relationship $\delta=\lambda_{sun}-\Omega$ is no longer satisfied, the constraint $\dot{\Omega}-n_{sun}=0$ cannot naturally guarantee that the value of δ is constant. To satisfy all conditions for heliotropic frozen orbits, we propose the following control strategy. As shown in Fig. 6, the diagram of the control strategy is divided into two parts. The upper part is used to choose a group of initial values satisfied for nominal heliotropic frozen orbits based on the simplified dynamical model, namely Eqs. (13). The lower part is used to adjust the values of the attitude angles and area-to-mass ratio to guarantee that the conditions for heliotropic frozen orbits are still satisfied under the full dynamical model, namely Eqs. (11). Three instructions are given to explain the lower part more clearly. First, the values of orbital elements and λ_{sun} at the next moment T should serve as new references to determine the values of three control parameters. Second, when η is determined by solving $\dot{\omega}=0$, another condition $\dot{\Omega}-n_{sun}=0$ will be naturally satisfied. Third, the proposed control strategy is a continuous control process in theory. However, if the integral step for Eqs. (11) is set as a relatively large value, such as one day, the control strategy can be regarded as a discrete control process, which is more feasible in practical engineering. The key in the proposed

control strategy is to keep the value of δ constant, which is impossible to be achieved in the discrete control process because the normal vector of sail surface cannot always keep up with the change of Ω. To improve the accuracy of the discrete control, a simple trick is proposed here. As shown in Fig. 7, suppose that a control manipulation is implemented at t_0, and the next control manipulation is implemented at t_0+T. If we adjust the normal vector of sail surface (the dashed red arrow) to guarantee δ equals π at t_0, δ will decrease to $\pi-n_{sun}T$ at t_0+T ($\dot{\Omega}$ equals n_{sun}), and the change range of δ is ($\pi-n_{sun}T$, π). However, if we adjust the normal vector of sail surface (the solid red arrow) to guarantee δ equals $\pi+ n_{sun}T/2$ at t_0, δ will decrease to $\pi-n_{sun}T/2$ at t_0+T, and the change range of δ turn out to be ($\pi-n_{sun}T/2$, $\pi+n_{sun}T/2$). Obviously, this trick benefits for keeping δ close to a wanted value, such as π. In addition, when T is chosen as one day, the maximum deviation $n_{sun}T/2$ equals about 0.5deg thanks to a small value of n_{sun}. The deviation of δ is so small that the heliotropic and frozen characteristics can be maintained for a long time, which is also verified in the following practical example.

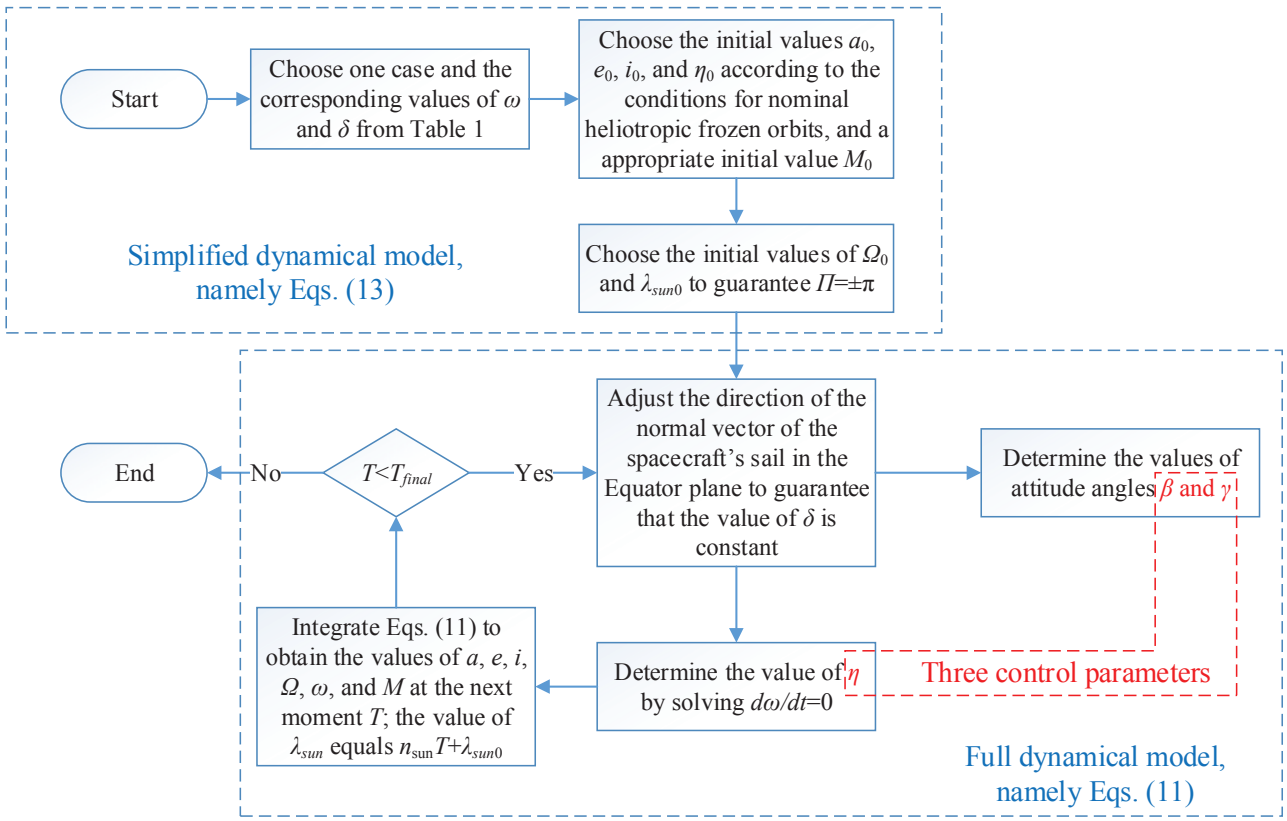

Fig. 6. Diagram of the control strategy for heliotropic frozen orbits.

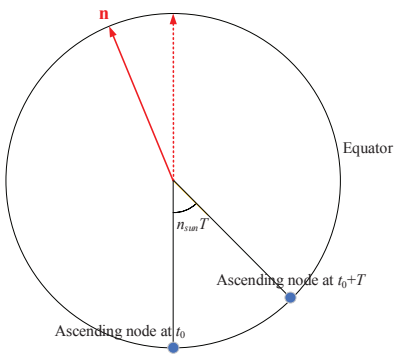

Fig. 7. The diagram of the trick in a discrete control process.

4.2. Practical Examples

Suppose that a solar sail spacecraft has a 25m×25m square sail and weighs 90kg, and the initial reflectivity coefficient of the sail is 1.8. Then, the initial effective area-to-mass ratio of this solar sail spacecraft is η_0=12.5m^2/kg. Suppose that this spacecraft is launched into a nominal heliotropic frozen orbit at the autumnal equinox of 2020, and the normal vector of sail surface points to the vernal equinox.

The initial values satisfied for the nominal heliotropic frozen orbits are chosen as a_0= 10560.27km, e_0= 0.1982, i_0= 2.0455, ω_0=0, Ω_0=0, M_0=0, δ_0=π, and λ_{sun0}=π. Then, we apply the proposed control strategy to this spacecraft and study its orbit in the next two years.

In the first scenario, the integral step for Eqs. (11) is set as one second so that we can regard this control as a continuous control process. It is necessary to study whether the heliotropic and frozen characteristics are maintained by checking the values of four indicators: three orbital elements e, i, ω, and the characteristic angle Π. As shown in Fig. 8a, the values of e, i and ω keep constant, which verifies the frozen characteristic of the orbit. In addition, the characteristic angle Π is nearly equal to π (the slight error should be caused by numerical calculations), which verifies the heliotropic characteristic of the orbit. Besides, Fig. 8b, c, and d demonstrate the rules of the change of three control parameters, which turn out to be periodic oscillations with a one-year period. The maximum adjustment value of attitude angle β exactly equals the obliquity angle of the ecliptic with respect to the equator, and it always occurs at summer and winter solstices each year. Fig. 9 gives a quantitative description of the solar radiation acceleration on the solar sail spacecraft, and it shows that the magnitude of the acceleration is 10^{-5}m/s^2. Because the normal vector of sail surface is controlled in the Equator plane, the acceleration component along the z-axis of S_g always equals zero. The red and blue lines represent the acceleration components along x-axis and y-axis of S_g, respectively, and the black line represents the total value of solar radiation acceleration. They display period changes and the period is one year as well.

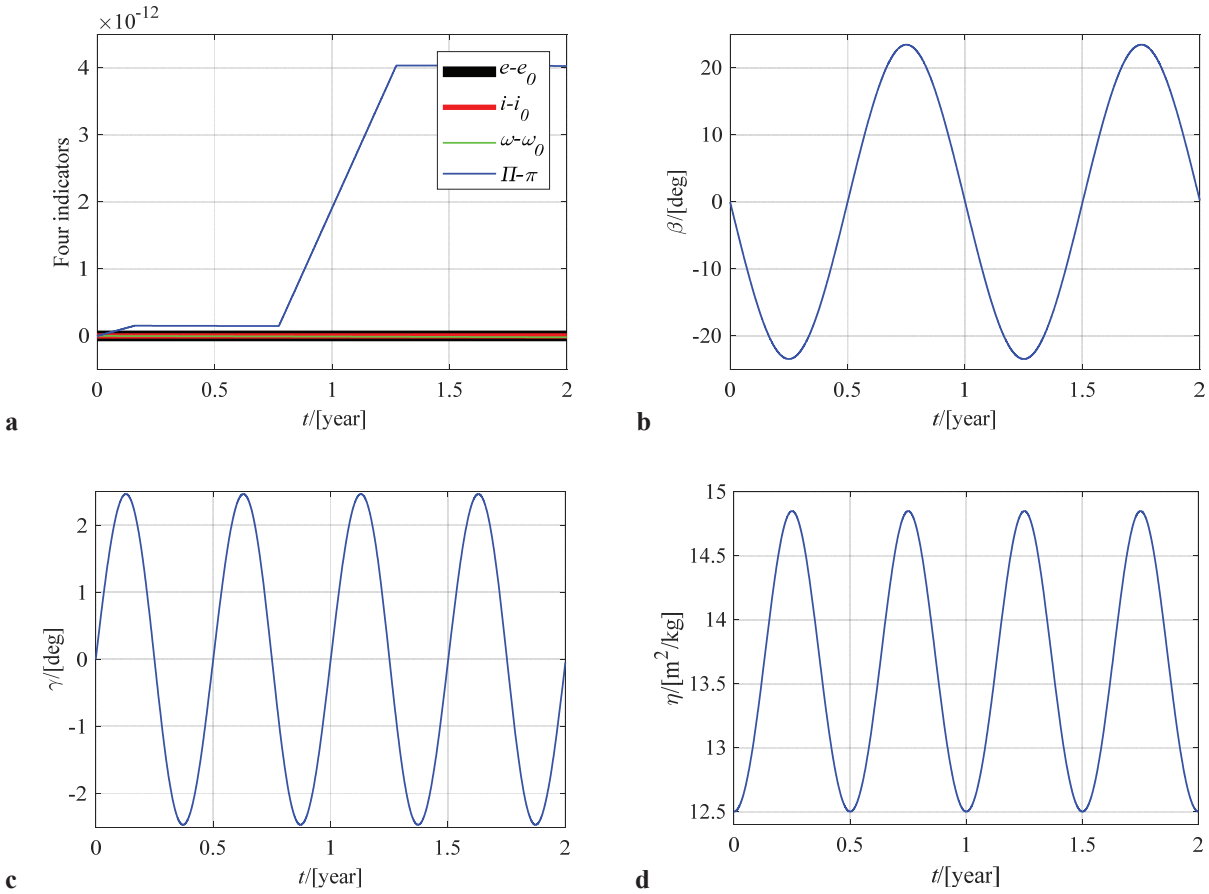

Fig. 8. The rules of the change of four indicators and three control parameters in the first scenario.

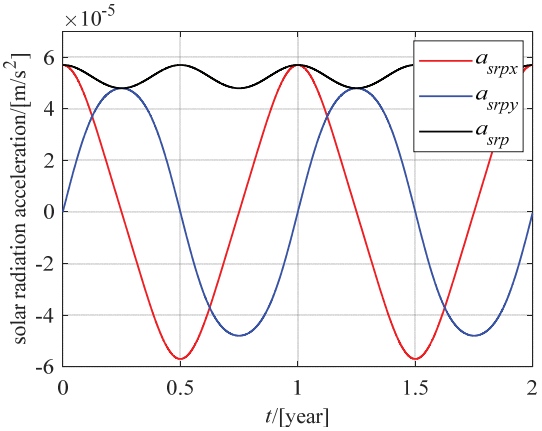

Fig. 9. The rules of the change of solar radiation acceleration in the first scenario.

In the second scenario, the integral step for Eqs. (11) is set as one day so that we can regard this control as a discrete control process. As shown in Fig. 10a, four indicators no longer keep constant and have a slight deviation. In addition, the magnified figure of the beginning part demonstrates oscillation

change feature of these indicators, especially e and i. However, the magnitude of deviation is less than 10^{-4}, which can be ignored from the viewpoint of engineering. As shown in Fig. 10b, attitude angle γ has the same change rule with that in the first scenario. Notice that the average value of γ is about 0.5deg in this scenario, while 0 deg in the former scenario. This difference is caused by the trick proposed for discrete control, which requires that the adjustment of γ is always $n_{sun}T/2$ (about 0.5deg when T is chosen as one day) larger than that in a continuous control. The change of attitude angle β is only determined by the motion of the Sun, resulting in the same rule with that in the former scenario. Because the deviations of four indicators are so slight that the change rules of effective area-to-mass ratio and SRP acceleration are almost the same with those in the former scenario. Here we do not repeat to plot their change rules.

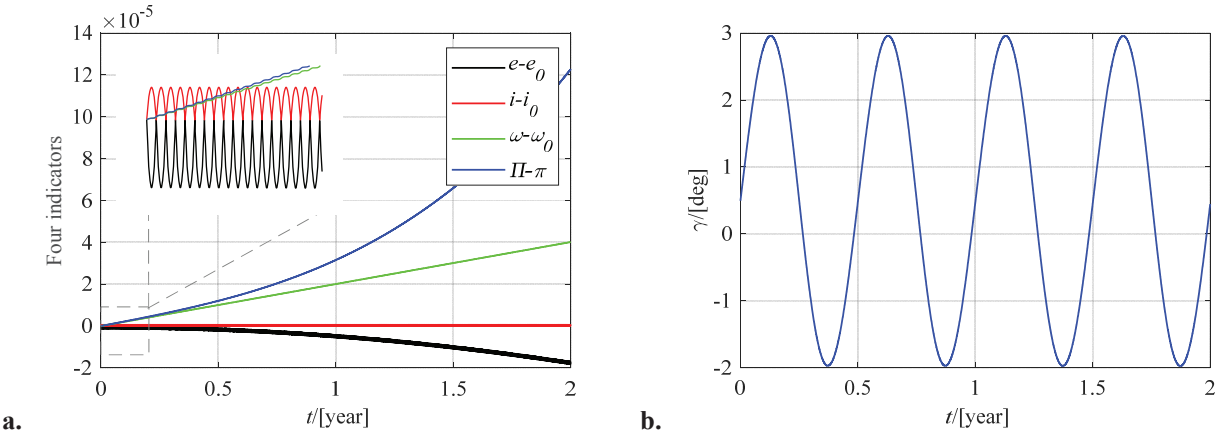

a. **b.**

Fig. 10. Changing rules of four indicators and attitude angle γ in the second scenario.

A spacecraft generally cannot be launched into a nominal heliotropic frozen orbit because of the injection error. In the third scenario, we choose the same initial values and control strategy with the second scenario, but injection errors Δa= 0.5km, Δe = 0.0005, Δi = 0.01deg, $\Delta\Omega$ = 0.01deg and $\Delta\omega$ = 0.01deg are added. Fig. 11a shows that the deviations of four indicators, especially Π, become larger than those in the second scenario. This means that heliotropic and frozen characteristics are influenced

by injection error, and the effect on heliotropic characteristic is more obvious. However, the magnitude of the largest deviation approaches 10^{-2}, which is still tolerable in engineering. Because the deviation tendency of Π is obvious, we can witness that there is a corresponding adjustment tendency of the average value of attitude angle γ in Fig. 11b. In addition, the change rules of effective area-to-mass ratio and SRP acceleration are almost the same as those in the former scenarios. Here we do not repeat to plot their change rules. In summary, this scenario verifies the robustness of the controlled heliotropic frozen orbit.

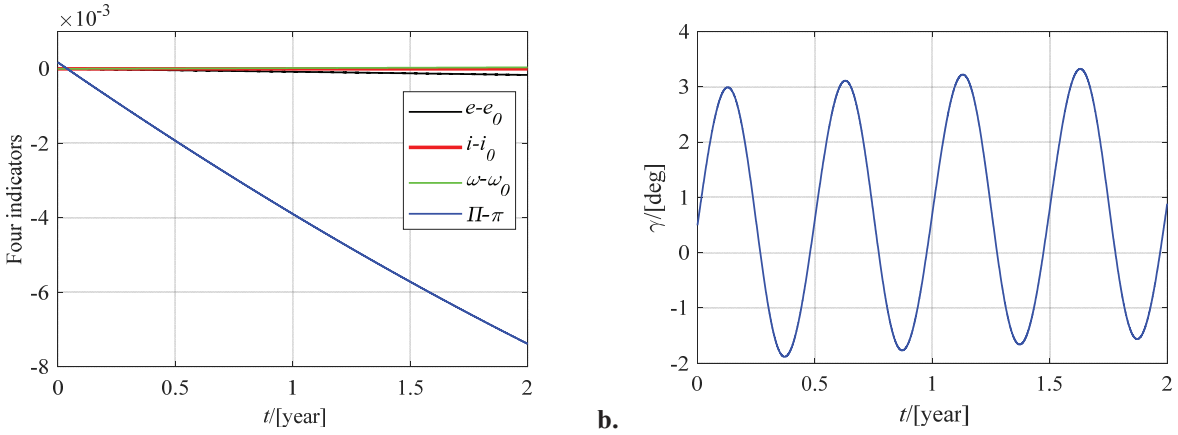

Fig. 11. Changing rules of four indicators and attitude angle γ in the third scenario.

4.3. Applications

Notice that the proposed heliotropic frozen orbits are medium earth orbits (MEO). Although low Earth orbits (LEO) and Geostationary Earth orbits (GEO) orbits are traditional venues for observations, MEO becomes attractive because of its potential to provide high spatial, temporal, and spectral resolution data [27]. The Jet Propulsion Laboratory (JPL) determined the optimal altitude for MEO observations as 10400km through numerous trade studies involving altitude, instrument complexity, coverage, radiation environment, coverage, spatial and temporal resolution, revisit time, data rates, data latency, downlink requirements, cost, and launch complexity [27]. Marco et al. [28] proposed

remote sensing application of Galileo constellation, through a bistatic Synthetic Aperture Radar system utilizing Galileo satellites on MEO as transmitters and Unmanned Aerial Systems as receives.

Here we give a detailed study on the controlled heliotropic frozen orbit in the second scenario to investigate its advantages in remote sensing and communication service. First, the effects of the oblateness of Earth and SRP on the period of the heliotropic frozen orbit can be neglected. For the given semi-major axis, the orbital period is calculated as $T = 2\pi/n = 3\text{h}$, which indicates that this orbit is a regression orbit and the regression period is one day. The left picture in Fig. 12 shows the sub-satellite point trajectory of the solar sail spacecraft. The trajectory begins to repeat after it flies around the Earth for 8 circles and can cover the area approximately from 60 degrees north altitude to 60 degrees south altitude. Second, the condition $\dot{\Omega} - n_{sun} = 0$ actually ensures sun-synchronous characteristic, which indicates that the local time is always the same when the solar sail spacecraft passes the same latitude in the same direction. Third, the right picture of Fig. 12 shows the position of the heliotropic frozen orbit around the Earth. This orbit provides better coverage during daylight hours since, at the apogee, which is always oriented in the direction of the Sun, the solar sail spacecraft moves slower than at the perigee, which is always oriented away from the Sun. This effect is also strengthened by the exploitation of SRP that allows an increase in the eccentricity of the Sun-pointing apogee. In this scenario, the solar sail spacecraft spends 2 hours in daylight while 1 hour in the night. A regression orbit can provide high-efficient and accurate service for a certain site. Frozen characteristic benefits for reducing orbit maintenance because the variations of orbital elements are theoretically zero. Sun-synchronous characteristic not only makes it much convenient to interact with the ground sites but also benefits for continuous earth observation by visible remote sensing method. Heliotropic characteristic guarantees sufficient working time in daylight, during which visible remote

sensing can be used and human have more frequent requirements for communication service as well.

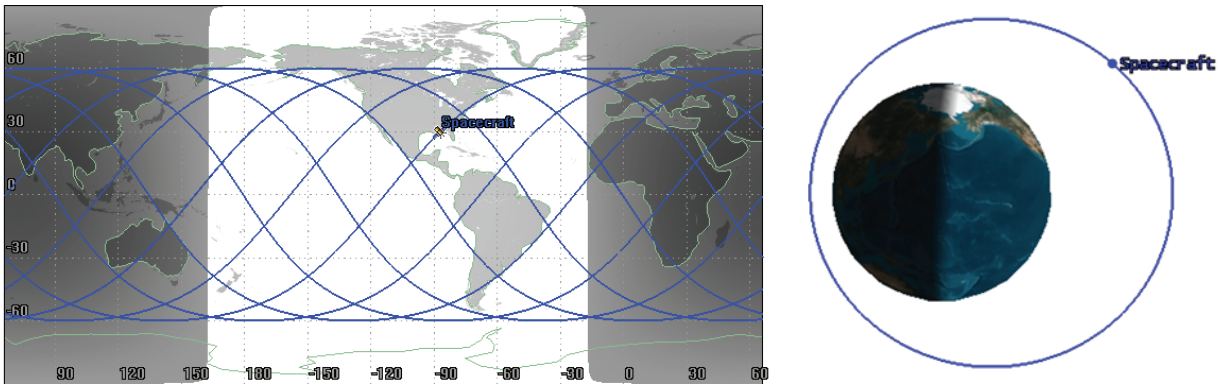

Fig. 12. The sub-satellite point trajectory of the spacecraft and the position of the heliotropic frozen orbit.

If we only change the condition $\Pi = \pm\pi$ in Eqs. (12) into $\Pi = \pi + \theta$, a group of new frozen orbits can also be generated using the same control strategy. They no longer strictly have heliotropic characteristic but is still sun-synchronous. Suppose that a spacecraft with the initial value of Ω_0 as 5deg namely θ equals -5deg and other parameters the same with the former one is added in the second scenario. These two spacecraft have the same period, ω and $\dot{\Omega}$, which can guarantee a natural formation flying between them. As shown in Fig. 13, the sub-satellite point trajectories of two spacecraft are parallel. They always pass through the same latitude together, and thus the connected line between them form a stable baseline for measurement. For example, two spacecraft in Fig. 13 can complete a mission of observing the Gulf of Mexico. Note that the distance between two spacecraft should be adjusted through setting the values of Ω_0 according to the practical requirements. Because solar sail spacecraft can afford the weight of an imaging payload, such as the moderate resolution imaging spectroradiometer (MODIS) and synthetically thinned aperture radiometer, they can easily accomplish the above mission. However, as for smart dust, its small size require them a larger and complex configuration to compose a complete imaging instrument together for a remote sensing mission. In addition, to utilize the swarm intelligence advantage of smart dust, we propose the

following communication service design based on the controlled heliotropic frozen orbits. As shown in Fig. 14, we can achieve a wide coverage of the Earth by establishing a series of frozen orbits via setting different values of Ω_0. It has been demonstrated that elliptical rings of spacecraft form wave-like patterns which circulate around the elliptical ring, with peaks in density at the apogee [29]. Thus, each orbit can provide basic venues for a swarm of smart dust for telecommunications, achieving enhanced coverage on the day-side of the Earth.

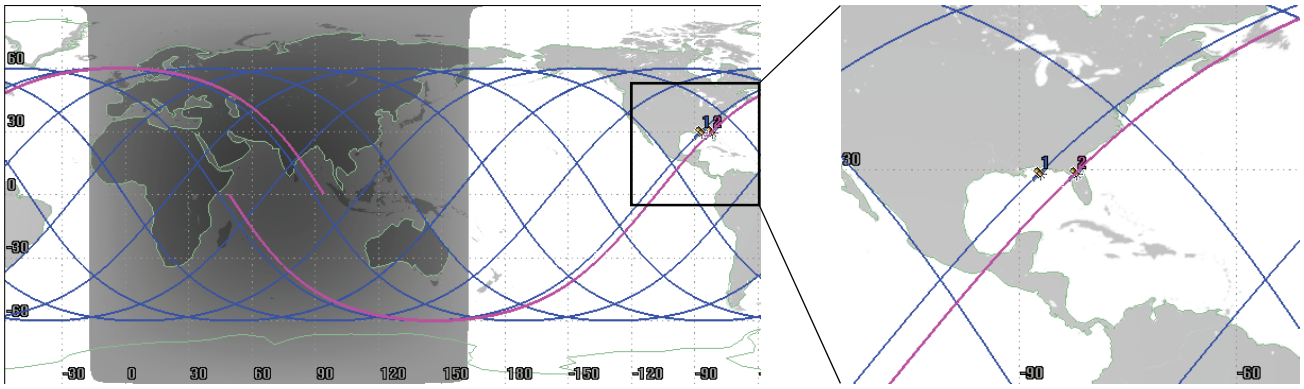

Fig. 13. Diagram of the mission of observing the Gulf of Mexico.

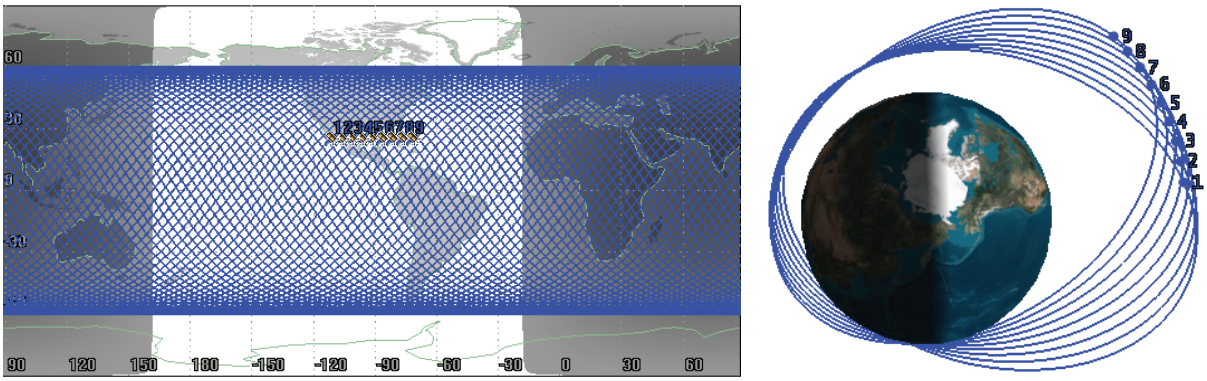

Fig. 14. Wide coverage of the Earth through a series of frozen orbits.

5. Conclusion

Aimed at high area-to-mass ratio spacecraft perturbed by J_2 and SRP, this paper proposed novel heliotropic frozen orbits which can be maintained by adjusting the attitude angles and the area-to-mass

ratio of the spacecraft. We first establish the dynamical model, based on Lagrange planetary equations and the J_2 and SRP disturbing functions. Through supposing the normal vector of the spacecraft's sail is always along the Earth-Sun line and the obliquity angle of the ecliptic with respect to the equator is ignored, we can obtain a series of nominal heliotropic frozen orbits from the simplified dynamical equations. Because the nominal heliotropic frozen orbits cannot be naturally maintained with the consideration of the obliquity angle of the ecliptic with respect to the equator, we propose a control strategy to maintain the nominal heliotropic frozen orbits. This paper provides a detailed procedure of the control strategy, including how to determine the values of three control parameters. Although the control strategy is theoretically a continuous control process, it can be regarded as a discrete control by setting the integral step of dynamical equations as a great value, such as one day.

Practical examples are provided to verify the heliotropic and frozen characteristics of the controlled orbits. Besides, the robustness of the controlled orbits for the injection error is also discussed by numerical simulations. Based on the proposed heliotropic frozen orbits, we can design orbits possessing regressive, frozen, Sun-synchronous and heliotropic characteristics at the same time. These advantages make heliotropic frozen orbits good options for Earth observation and communication service. However, there are still some practical issues worthy study, such as how to compose an imaging instrument by smart dust.

Acknowledgment

This work was supported by the National Natural Science Foundations of China (11432001 and 11772024), the European Research Council (ERC) under the European Union's Horizon 2020 research (227571), and the Innovation Practice Foundation of Beihang University (YCSJ-01-2018-08)

References

[1]. Colombo, C., Lücking, C., and McInnes, C. R., "Orbital dynamics of high area-to-mass ratio spacecraft with J_2 and solar radiation pressure for novel Earth observation and communication services," *Acta Astronautica*, 81(1): 137-150, 2012.

[2]. Bewick, R., Lücking, C., Colombo, C., Sanchez, J. P., and McInnes, C. R., "Heliotropic dust rings for Earth climate engineering," *Advances in Space Research*, 51(7): 1132-1144, 2013.

[3]. Luo, T., Xu, M., and Colombo, C., "Dynamics and control of high area-to-mass ratio spacecraft and its application to geomagnetic exploration," *Acta Astronautica*, 145: 424-437, 2018.

[4]. McInnes, C. R., "A continuum model for the orbit evolution of self-propelled 'smart dust' swarms," *Celestial Mechanics and Dynamical Astronomy*, 126(4): 501-517, 2016.

[5]. McInnes., C.R., *Solar Sailing: Technology, Dynamics and Mission Applications*, Springer, Berlin, 1999, Chap. 5.

[6]. Johnson, L., Whorton, M., Heaton, A., Pinson, R., Laue, G., and Adams, C., "NanoSail-D: A Solar Sail Demonstration Mission," *Acta Astronautica*, 68(5): 571–575, 2011.

[7]. Tsuda, Y., Mori, O., Funase, R., Sawada, H., Yamamoto, T., Saili, T., Endo, T., and Kawaguchi, J., "Flight Status of IKAROS Deep Space Solar Sail Demonstrator," *Acta Astronautica*, 69(9): 833–840, 2011.

[8]. Biddy, C., and Svitek, T., "LightSail-1 Solar Sail Design and Qualification," *Proceedings of the 41st Aerospace Mechanisms Symposium, Jet Propulsion Lab*., National Aeronautics and Space Administration, Pasadena, CA, 451–463, 2012.

[9]. Firuzi, S., and Gong, S., "Refractive sail and its applications in solar sailing," *Aerospace Science and Technology*, 77: 362-372, 2018.

[10]. Felicetti, L., and Santoni, F, "Nanosatellite swarm missions in low Earth orbit using laser propulsion," *Aerospace Science and Technology*, 27(1): 179-187, 2013.

[11]. Hamilton, D. P., and Krivov, A. V., "Circumplanetary dust dynamics: Effects of solar gravity, radiation pressure, planetary oblateness, and electromagnetism," *Icarus*, 123(2): 503-523, 1996.

[12]. Colombo, C., and McInnes, C., "Orbital Dynamics of "Smart-Dust" Devices with Solar Radiation Pressure and Drag," *Journal of Guidance, Control, and Dynamics*, 34(6): 1613-1631, 2011.

[13]. Früh, C., and Jah, M. K., "Attitude and orbit propagation of high area-to-mass ratio (HAMR) objects using a semi-coupled approach," *The Journal of the Astronautical Sciences*, 60(1): 32-50, 2013.

[14]. Zhao, Y., Gurfil, P., and Zhang, S., "Long-Term Orbital Dynamics of Smart Dust," *Journal of Spacecraft and Rockets*, 55(1): 125-142, 2017.

[15]. Mengali, G., and Quarta, A. A., "Heliocentric trajectory analysis of Sun-pointing smart dust with electrochromic control," *Advances in Space Research*, 57(4): 991-1001, 2016.

[16]. Mengali, G., Quarta, A. A., and Denti, E., "Relative Motion of Sun-Pointing Smart Dust in Circular Heliocentric Orbits," *Journal of Guidance, Control, and Dynamics*, 41(4): 1015-1020, 2017.

[17]. Colombo, C., and McInnes, C. R., "Constellations of inclined heliotropic orbits for enhanced earth coverage," In 63rd International Astronautical Congress (IAC), Curran Associates, 5568-5578, 2012.

[18]. Lantukh, D., Russell, R. P., and Broschart, S., "Heliotropic orbits at oblate asteroids: balancing solar radiation pressure and J_2 perturbations," *Celestial Mechanics and Dynamical Astronomy*, 121(2): 171-190, 2015.

[19]. Russell, R. P., Lantukh, D., and Broschart, S. B., "Heliotropic Orbits with Zonal Gravity and Shadow Perturbations: Application at Bennu," *Journal of Guidance, Control, and Dynamics*, 1925-1933, 2016.

[20]. Chobotov, V. A., *Orbital Mechanics*, American Institute of Aeronautics and Astronautics, Inc., Washington, 251–252, 291–296, 1991.

[21]. Aorpimai, M., & Palmer, P. L., "Analysis of frozen conditions and optimal frozen orbit insertion," *Journal of guidance, control, and dynamics*, 26(5): 786-793, 2003.

[22]. Lee, B. S., and Lee, J. S., "Selection of initial frozen orbit eccentricity and evolution of the orbit due to perturbations," *Journal of the Korean Society for Aeronautical and Space Sciences*, 25(1): 126-126, 1997.

[23]. Park, S. Y., and Junkins, J., "Orbital mission analysis for a lunar mapping satellite," In Astrodynamics Conference 3717, 1994.

[24]. Roh, K. M., Luehr, H., Rothacher, M., and Park, S. Y., "Investigating suitable orbits for the Swarm constellation mission-The frozen orbit," *Aerospace Science and Technology*, 13(1): 49. 2009.

[25]. Krivov, A. V., Sokolov, L. L. and Dikarev, V. V., "Dynamics of Mars-Orbiting Dust: Effects of Light Pressure and Planetary Oblateness," *Celestial Mechanics and Dynamical Astronomy*, 63(3): 313-339, 1995.

[26]. Brouwer, D. and Clemence, G., *Methods of Celestial Mechanics*, Academic Press, New York, 1961, Chap. 15.

[27]. Gerber, A. J., Tralli, D. M., and Bajpai, S. N., "Medium Earth Orbit (MEO) as an operational observation venue for NOAA's post GOES-R environmental satellites," *Proc Spie*, 5659: 261-271, 2005.

[28]. Marco, D., Renga, A., and Graziano M. D., "Earth observation with MEO transmitters and UAS receivers: A potential utilization of Galileo constellation," *Acta Astronautica*, 94(1): 93-103, 2014.

[29]. McInnes, C. R., Colombo C., "Wave-like pattern in an elliptical satellite ring," *Journal of guidance, control, and dynamics*, 36(6): 1767-1771, 2013.